RSC Advances

PAPER

View Article Online
View Journal | View Issue

Cite this: *RSC Adv.*, 2017, **7**, 51046

A novel Nb_2O_5/Bi_2WO_6 heterojunction photocatalytic oxidative desulfurization catalyst with high visible light-induced photocatalytic activity

Jing Wu, Jian Li, Jin Liu, Jin Bai and Lina Yang *

A novel Nb_2O_5/Bi_2WO_6 heterojunction catalyst was successfully synthesized *via* a one-pot solvothermal process. The catalyst was characterized by X-ray diffraction (XRD), scanning electron microscopy (SEM) with the corresponding XEDS energy mapping, UV-vis diffuse reflection spectra (UV-vis DRS), Fourier transform infrared (FTIR) spectroscopy and X-ray photoelectron spectroscopy (XPS). The photocatalytic oxidative desulfurization performances of the prepared samples were studied with DBT as the model sulfur compound under visible light irradiation. Results indicated that the Nb_2O_5/Bi_2WO_6 exhibited considerably higher activity than pure Nb_2O_5 and Bi_2WO_6 and the desulfurization rate achieved 99% after visible light irradiation for 120 min. The catalyst also possessed good stability so that the desulfurization rate remained about 90% after seven cycle times and then the crystal structure of the catalyst has barely changed. Such enhanced photocatalytic activity is mainly attributed to the effective separation of photogenerated electron–hole pairs on Nb_2O_5/Bi_2WO_6 heterojunction. Moreover, the synergistic effects of this photocatalytic oxidation and the extraction with the methanol as the solvent played an indispensable role in the desulfurization.

Received 4th September 2017
Accepted 24th October 2017

DOI: 10.1039/c7ra09829d

rsc.li/rsc-advances

1. Introduction

Sulfur oxides (SO_x) released from the combustion of transportation fuels lead to atmospheric haze, acid rain and many other environmental issues.[1–3] Numerous countries have promulgated regulations to restrict the sulfur content in fuels, some of them demanding that the sulfur content of diesel and gasoline must be less than 10 $\mu g\ g^{-1}$ even sulfur-free for regular gasoline.[4] Therefore, to meet the demand of liquid fuels with ultra-low sulfur content, the development of deep desulfurization technologies has become a hot subject nowadays.

It is well known that applications of visible light in addressing environmental issues have attracted more and more attention.[5–8] In the same way photocatalytic oxidative desulfurization (PODS) method, especially the visible light-induced PODS, as one of the promising new method for deep desulfurization of fuels has gained great interest because of its mild operation conditions and resultant low investment and operating costs.[9] Various studies on the PODS process have been reported in the past few years.[10–12] So many photocatalysts, such as TiO_2,[13] $TiO_2/g\text{-}C_3N_4$,[14] CeO_2/TiO_2,[12] Bi_2WO_6,[15] $Bi_2W_{1-x}Mo_xO_6$/montmorillonite (MMT)[16] and so on, have been applied in the PODS process.

Nevertheless, developing more efficient visible light photocatalytic material for the desulfurization is still an imperative challenge for researchers. Niobium oxide (Nb_2O_5), as n-type transition oxide semiconductor, has been widely used in many fields, such as photocatalytic hydrogen production, photodegradation of organic contaminants and so on.[17,18] However, for the single-phase Nb_2O_5, the low quantum yield caused by the rapid recombination of photogenerated electron and hole limited their application. To address this concern, some researchers loaded some amounts of metal or non-metal to Nb_2O_5. Some reports on combining Nb_2O_5 with other semiconductor to synthesize the heterojunction have also been found in the field of photocatalysis.[19–22] The heterojunction can inhibit the recombination of photogenerated hole–electron pair consequently the heterojunction which was constructed based on the different Fermi level of Nb_2O_5 from another semiconductor has been proven more effective than the loaded catalysts. Recently, a few Nb_2O_5 composited heterojunctions have been reported, such as Ag_3PO_4/Nb_2O_5,[21] Nb_2O_5/TiO_2,[22] $Nb_2O_5/SrNb_2O_6$ [23] and so on. And such catalysts were mostly applied in the degradation of polluted water under visible light irradiation. By now seldom reports on the application of Nb_2O_5 containing heterojunction catalyst in PODS were found. Hence finding more companions to construct heterojunction catalysts and try to apply it in PODS is extremely urgent.

College of Chemistry, Chemical Engineering and Environmental Engineering, Liaoning Shihua University, 113001, Liaoning, P. R. China. E-mail: yanglnzg@163.com

In recent years, Bi_2WO_6 attracted great attention for its excellent visible light induced photocatalytic activity, chemical and thermal stability and non-toxicity.[24] Unfortunately, its application is still limited because of the high recombination rate of photogenerated holes and electrons. Many attempts to enhance photocatalytic activities by manufacturing Bi_2WO_6 composite have also been reported.[25–27] To our excitement the band structures of Bi_2WO_6 and Nb_2O_5 interlaced,[21,25] which is in favour of promoting the separation of the photogenerated carriers, as a result Bi_2WO_6 will be an appropriate candidate to construct the heterojunction with Nb_2O_5.[28] To the best of our knowledge, the Nb_2O_5/Bi_2WO_6 photocatalyst has not been reported.

Herein a novel Nb_2O_5/Bi_2WO_6 heterojunction photocatalyst was prepared and applied in PODS with dibenzothiophene (DBT) as a model sulfur compound. Nb_2O_5/Bi_2WO_6 owns enhanced photocatalytic activity over both Nb_2O_5 and Bi_2WO_6 and it also has fine stability. The mechanism of its photocatalysis was proposed and proved. The synergistic effects of the photocatalytic oxidation and the extraction were also confirmed.

2. Experimental

2.1 Materials

All the chemicals were of analytical grade and they were used directly in our experiments without any further purification. Bismuth nitrate ($Bi(NO_3)_3\cdot 5H_2O$), niobium pentoxide (Nb_2O_5), ammonium tungstate ($(NH_4)_5H_5[H_2(WO_4)_6]\cdot H_2O$) were purchased from Medicine Group Chemical Reagent Co., Ltd. Nitric acid (HNO_3), methyl alcohol (CH_3OH) hydrogen peroxide (H_2O_2), dodecane ($C_{12}H_{16}$) were purchased from Tianjin regent chemicals Co., Ltd. DBT was purchased from Aladdin Bio-Chem Technology Co., Ltd. The deionized water was used throughout.

2.2 Preparation of Nb_2O_5/Bi_2WO_6 catalysts

The Nb_2O_5/Bi_2WO_6 was prepared with the solvothermal technique. In a typical synthesis procedure, 30 mL nitric acid solution of $Bi(NO_3)_3\cdot 5H_2O$ (the molar ratio of $Bi(NO_3)_3\cdot 5H_2O$ to HNO_3 is 1.00 : 0.17) and 20 mL solution of $(NH_4)_5H_5[H_2(WO_4)_6]\cdot H_2O$ (the molar ratio of W to Bi is 1 : 2 and the dissolving temperature is 60 °C) were prepared respectively. Then the later was added into the former drop by drop to form the suspension. A certain amount of Nb_2O_5 was added into the resulting suspension after vigorously stirring for 2 h at 40 °C. This mixture was stirred for another 0.5 h and then transferred into a Teflon-lined autoclave for solvothermal treatment at 160 °C for 12 h. Subsequently, the system was cooled to room temperature naturally; the resulting precipitate was filtrated, washed with deionized water until the solution neutral, and then dried at 80 °C for 8 h. The mass percent of Nb_2O_5 in Nb_2O_5/Bi_2WO_6 were controlled to be 1, 5 and 10 wt%, which were designated as x wt% Nb_2O_5/Bi_2WO_6 ($x = 1, 5, 10$). For comparison, the bulk Bi_2WO_6 was also prepared and the synthetic process followed the above technique without Nb_2O_5.

2.3 Characterization of catalysts

X-ray diffraction (XRD) patterns were obtained on a D/max-IIIA X-ray diffractometer (Rigaku, Japan) with Cu-Kα radiation operating at 35 kV and 30 mA. Fourier Translation Infrared Spectra (FTIR) spectra were recorded on a Nicolet 380 spectrometer (Thermo Fisher Scientific) in the range of 4000–400 cm^{-1}. The optical diffuse reflectance spectra were recorded with UV-vis-NIR Spectrophotometer (Agilent, Cary 2450) over a range of 400–800 nm. Surface morphologies were investigated on the scanning electron microscopy (SEM) (Hitachi SU 8000) operated at an acceleration voltage of 15 kV and the elements of the sample were analyzed by corresponding XEDS energy mapping. X-ray photoelectron spectroscopy (XPS) was obtained on an ESCALAB 250 spectrometer at room temperature and Al-Kα irradiation to determine the chemical states of Bi, W, Nb, and O atoms in the prepared samples.

2.4 Photocatalytic oxidative desulfurization

Model fuel with the sulfur concentration of 200 μg g^{-1} was prepared by dissolving DBT in the dodecane. PODS reaction was operated in a beaker with magnetic stirring at ambient temperature. Two 5 W 420 nm LED lamps were used as the visible light sources and the distance from the light sources to the beaker is about 10 cm.

Typically, 20 mL model fuel was added firstly into a 100 mL beaker, and then some amount of CH_3OH (calculated in the volume ratio to the model fuel of 1 : 1), catalyst (calculated in the mass percent of 1 wt% in the model fuel) and H_2O_2 (30 wt%, calculated in O/S molar ratio of 10) were also introduced in order. The beaker was placed in the dark with constant magnetic stirring for 30 min firstly to establish adsorption–desorption equilibrium of DBT on catalysts. Then the PODS proceed under the visible light irradiation. The samples were withdrawn periodically every 20 min from the upper phase and detected by WK-2D microcoulometric detector after high speed centrifuge. The operating parameter was followed by integral resistance 400 Ω, bias voltage between 148 and 149 mV, burning furnace temperature 850 °C, evaporation section temperature 750 °C, and stable section temperature 650 °C, the oxygen flow rate 150 mL min^{-1} and nitrogen flow rate 260 mL min^{-1}. In addition, the model fuel before and after PODS and methanol phase after PODS were analysed by gas chromatography-mass spectrometer (GC-MS, Agilent 7890A). The major measuring conditions were as follows: injection port temperature 250 °C; temperature program of the oven 100 °C and the detector temperature was 300 °C.

The desulfurization rate (η) of model fuel was calculated by eqn (1):

$$\eta = (1 - C/C_0) \times 100\% \quad (1)$$

where C_0 is the sulfur content of the feed, and C is the sulfur content of the product after photocatalytic reaction.

2.5 Stability test

Catalyst was separated from the reaction mixture by the filtration and washing with the deionized water, dried at 80 °C for 12 h and then directly used for the next run.

2.6 Active species trapping experiments

In the typical PODS process the model fuel, CH_3OH, 5 wt% Nb_2O_5/Bi_2WO_6 photocatalyst and H_2O_2 were added into the beaker in order, then 1.0 mM isopropanol (IPA), *p*-benzoquinone (*p*-BQ) and disodium ethylenediaminetetraacetate (EDTA-2Na) were also added into the beaker respectively for detecting hydroxyl radicals ($^{\bullet}OH$), superoxide radicals ($^{\bullet}O_2^-$) and holes (h^+).[29]

3. Results and discussion

3.1 Characterizations

3.1.1 XRD analysis. The XRD patterns of 5 wt% Nb_2O_5/Bi_2WO_6, pure Nb_2O_5 and pure Bi_2WO_6 were shown in Fig. 1. The major diffraction peaks of pure Bi_2WO_6 at $2\theta = 10.7°$, 28.3°, 32.9°, 47.2°, 55.9° and 58.6° due to (020), (131), (002), (202), (133), and (262) respectively, matched well with the reflection planes of the orthorhombic Bi_2WO_6 phase (JCPDS, PDF #39-0256).[30,31] The diffraction peaks of pure Nb_2O_5 correspond to the orthorhombic structure of Nb_2O_5 (JCPDS, PDF #27-1003). The high and sharp diffraction peaks of these two samples indicated the well-defined crystallinity. Compared with the bulk Bi_2WO_6 the corresponding characteristic peaks for 5 wt% Nb_2O_5/Bi_2WO_6 present no shift, suggesting that Nb_2O_5 is not incorporated into the lattice of Bi_2WO_6, but deposited on the surfaces.[32] Moreover, only the diffraction peaks of Bi_2WO_6 and Nb_2O_5 were found for 5 wt% Nb_2O_5/Bi_2WO_6, which rule out the existence of another phase.

3.1.2 SEM analysis. The morphology and microstructure of samples were shown in Fig. 2. The SEM images of the fabricated Bi_2WO_6 were displayed in Fig. 2A and B, here microspheres with a diameter of around 2–3 μm looks like flowers with interlaced petals, such morphology is similar to the reported results for Bi_2WO_6.[33] The 'petals' in the 'flower' are factually the two-dimensional nanosheets and their surface is smooth without defects or holes. After the depositing of Nb_2O_5, the size of the resulting 5 wt% Nb_2O_5/Bi_2WO_6 nanoparticles (Fig. 2C and D) have no obvious change, however, the small accumulated Nb_2O_5 nanoparticles were clearly seen in the intervals between the Bi_2WO_6 nanosheets. As far as the Nb_2O_5 with no accumulation we are not sure of its existence only based on the SEM image. Furthermore, the corresponding XEDS energy mapping of 5 wt% Nb_2O_5/Bi_2WO_6 were tested and the results were shown in Fig. 2E–H. Results for elements including Bi, W, O and Nb further indicated that the Nb_2O_5 particles were successfully introduced into Bi_2WO_6, which are consistent with results of XRD. Based on distribution result of Nb in XEDS, we can conclude the well dispersed nanoparticles also existed all over the sample beside the accumulated ones, which is favorable for the improvement of the catalytic performance of the catalyst.

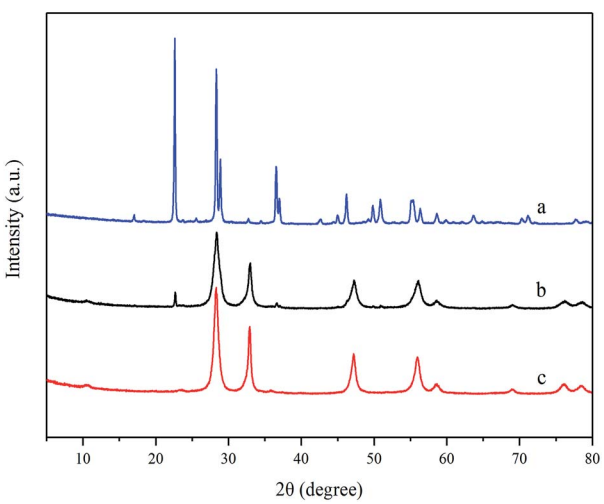

Fig. 1 XRD patterns of different samples: (a) Nb_2O_5; (b) 5 wt% Nb_2O_5/Bi_2WO_6; (c) Bi_2WO_6.

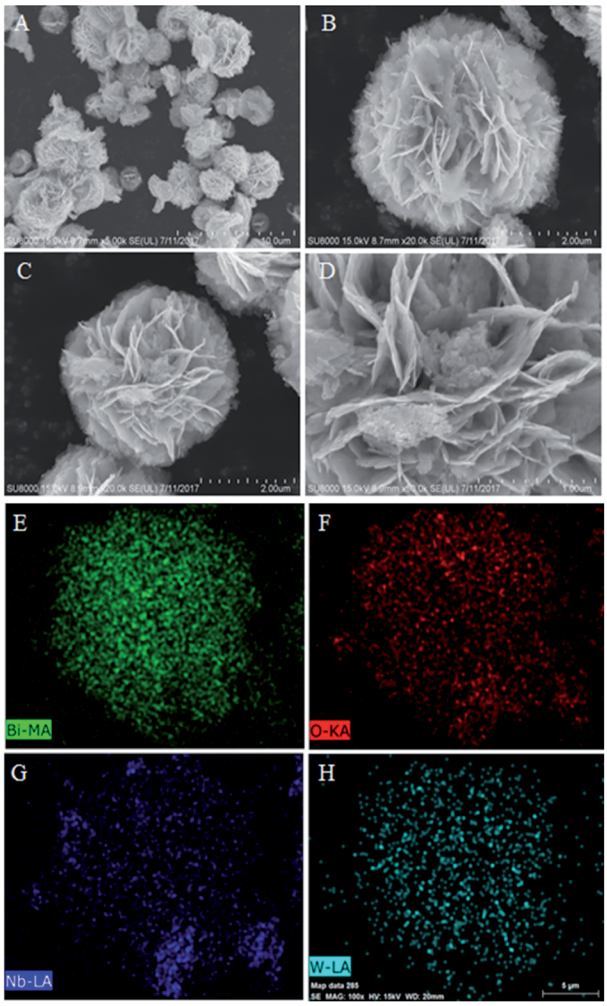

Fig. 2 SEM images of the samples (A–B) Bi_2WO_6; (C) 5 wt% Nb_2O_5/Bi_2WO_6; (D) enlarged image of 5 wt% Nb_2O_5/Bi_2WO_6; (E–H) the corresponding XEDS energy mapping of 5 wt% Nb_2O_5/Bi_2WO_6.

3.1.3 UV-vis analysis. The optical properties of the photocatalyst were investigated using UV-visible diffuse reflectance spectroscopy. As shown in Fig. 3A, it is clear that the Bi_2WO_6 sample exhibits the strong photoabsorption in the UV light region and the weak photoabsorption in the visible light region shorter than 470 nm. The intrinsic absorption of Nb_2O_5 is

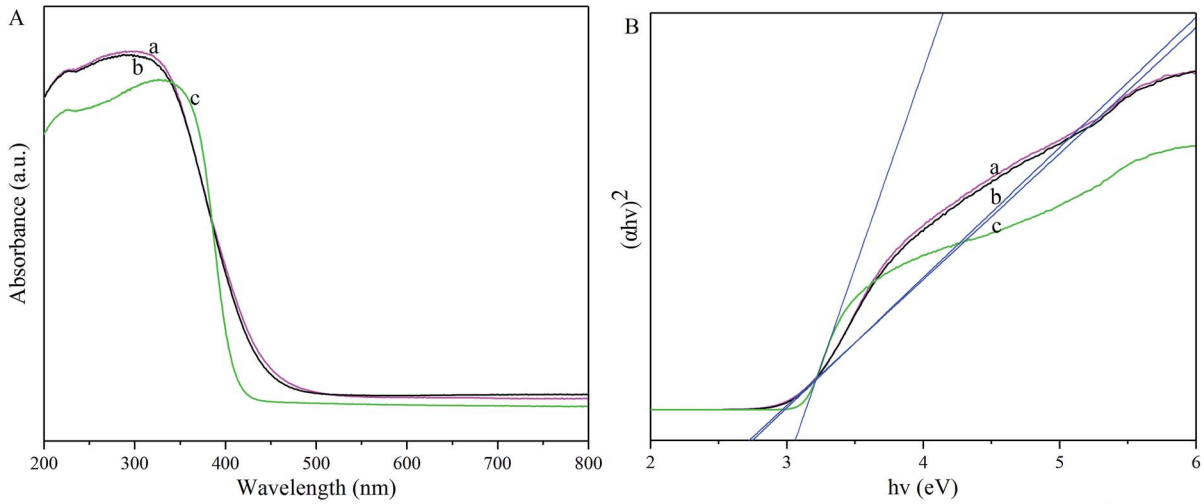

Fig. 3 (A) UV-vis diffuse reflectance spectra of the samples and (B) estimated band gap of photocatalyst by plots of $(\alpha h\nu)^2$ *vs.* photon energy ($h\nu$) (a) Bi_2WO_6; (b) 5 wt% Nb_2O_5/Bi_2WO_6; (c) Nb_2O_5.

observed in the ultraviolet region and the absorption was also observed in the visible light region. Compared with Nb_2O_5, the intensity of the absorption peak for 5 wt% Nb_2O_5/Bi_2WO_6 increased, which suggested the better separation of electron–hole pairs, leading to the enhanced photocatalytic activity. Meanwhile, the slight red shift of the absorption edge for 5 wt% Nb_2O_5/Bi_2WO_6 proved the formation of the heterojunction.[12] The bandgap energy of the samples can be estimated using the Kubelka–Munk function as the following formula:

$$\alpha h\nu = A(h\nu - E_g)^{n/2} \quad (2)$$

where α, h, ν, A and E_g are absorption coefficient, Planck constant, light frequency, a constant and band gap energy, respectively. The value of n is determined by the transition type ($n = 4$ and 1 for indirect and direct absorption, respectively).[34] The n value is 1 for Bi_2WO_6 and Nb_2O_5 with indirect transition.[29,35] Plots of $(\alpha h\nu)^2$ *versus* $h\nu$ were listed in Fig. 3B, the intercepts of the tangents of the plots give a good approximation to the band gap energy for the materials. The band gaps for Bi_2WO_6, Nb_2O_5 and 5 wt% Nb_2O_5/Bi_2WO_6 were estimated as 2.73 eV, 3.07 eV and 2.75 eV, respectively. Here Nb_2O_5 is orthorhombic, the band gap of it is less than 3.2 eV, which is consistent with the related report.[36] Based on the band gaps it can be concluded that here Bi_2WO_6 is an apparent visible light introduced sample. The sensitive wavelength for Nb_2O_5 is near to the UV region, however, the introducing of small amount of Nb_2O_5 into Bi_2WO_6 can't make 5 wt% Nb_2O_5/Bi_2WO_6 to be UV sensitive sample.

3.1.4 FTIR analysis. The FTIR spectra can provide some valuable surface chemical information, and the FTIR spectra of Bi_2WO_6 and Nb_2O_5/Bi_2WO_6 (the percent of Nb_2O_5 are in 1–10 wt%) samples were shown in Fig. 4. The main absorption peaks between 500 and 1200 cm^{-1} can be ascribed to stretching vibration of Bi–O and W–O, and bridging stretching modes of W–O–W.[37] In detail, the absorption peak of 716 cm^{-1} is attributed to the stretching vibrations of the W–O–W bonds, while the weak absorption peak at 822 cm^{-1} can be ascribed to the asymmetric stretching vibrations of the O–W–O bonds.[38] The peak at 576 cm^{-1} is attributed to the stretching vibration of the W–O bond and that at 730 cm^{-1} is assigned to the stretching vibration modes of Bi–O bonds, which are overlapped with the stretching vibration of the W–O–W bond at 716 cm^{-1}.[39] Results verified that samples have [WO_6] cluster distortions in their crystal lattices after the deposition of Nb_2O_5. With increase of the mass concentration of Nb_2O_5 in Nb_2O_5/Bi_2WO_6 the intensities of the peaks at 576 cm^{-1} and 822 cm^{-1} both decreased, which suggests the chemical interaction between Nb_2O_5 and Bi_2WO_6. There are no obvious absorption peaks of Nb–Nb–O and $[-O-Nb-O]_n$ displayed in the patterns,[40] which could be attributed to the limited amount of Nb_2O_5 and the absorption peaks overlapping with O–W–O.

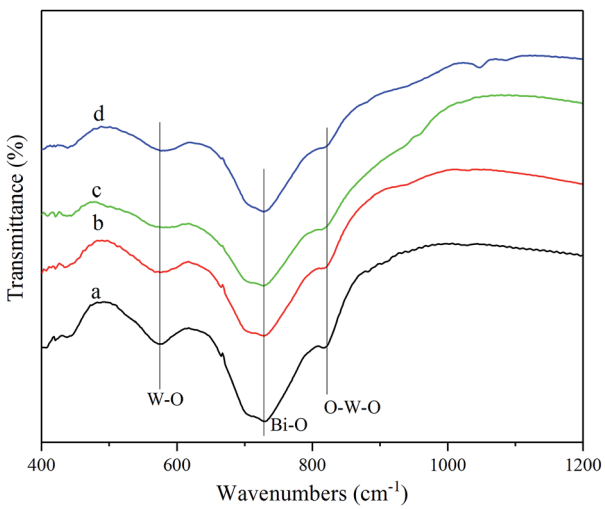

Fig. 4 FTIR spectra of the Bi_2WO_6 and Nb_2O_5/Bi_2WO_6 samples (a) Bi_2WO_6; (b) 1 wt% Nb_2O_5/Bi_2WO_6; (c) 5 wt% Nb_2O_5/Bi_2WO_6; (d) 10 wt% Nb_2O_5/Bi_2WO_6.

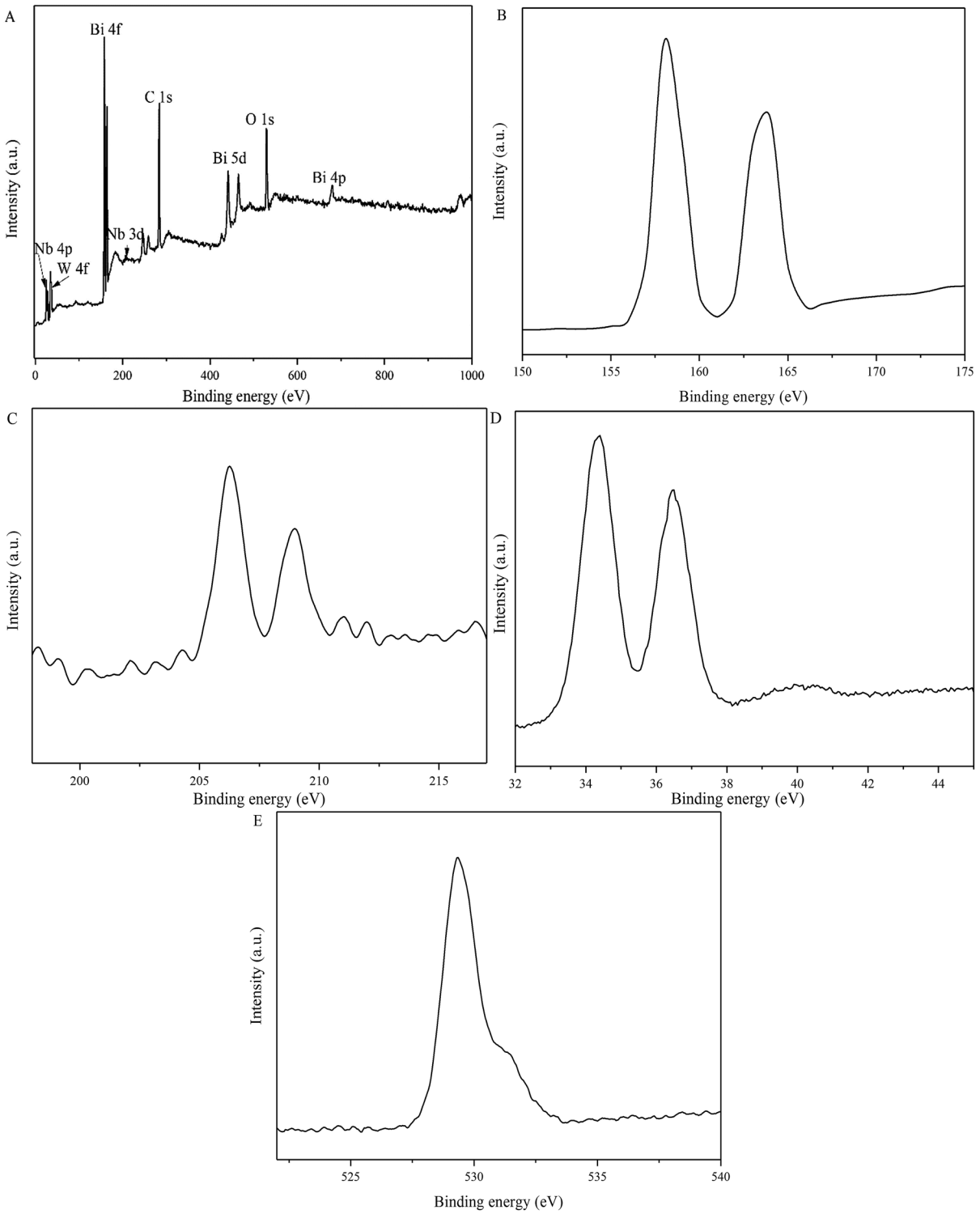

Fig. 5 XPS spectra of 5 wt% Nb_2O_5/Bi_2WO_6 heterostructured photocatalyst (A) full spectra; (B) Bi 4f; (C) Nb 3d; (D) W 4f; (E) O 1s.

3.1.5 XPS analysis. To further confirm the surface element composition and the interaction between Nb_2O_5 and Bi_2WO_6, XPS results of 5 wt% Nb_2O_5/Bi_2WO_6 were obtained and displayed in Fig. 5. All peak positions were calibrated by C 1s peak at 284.8 eV. The typical XPS survey spectra (Fig. 5A) showed that the Bi, W, Nb and O elements all existed in the sample, beside adventitious carbon contamination.[41] High resolution spectra of different elements were shown in Fig. 5B–E. Among them, the binding energy values of Bi 4f observed at 158.1 eV and 164 eV were ascribed to Bi $4f_{7/2}$ and Bi $4f_{5/2}$ spin states, respectively, corresponding to the oxidation state of Bi^{3+} in Bi_2WO_6.[16] The peaks of Nb 3d located at 206.9 eV and 208.5 eV were assigned to

Nb $3d_{5/2}$ and Nb $3d_{3/2}$ spin states, respectively, suggesting that Nb exists in the chemical state of Nb^{5+}. Two peaks at binding energies of 34.4 eV and 36.5 eV were assigned to W $4f_{5/2}$ and W $4f_{7/2}$, respectively, which reveals the chemical valence state for W^{6+} in Bi_2WO_6.[42] The binding energy of 529.3 eV for O 1s in 5 wt% Nb_2O_5/Bi_2WO_6 is slightly lower than that reported one for pure Bi_2WO_6.[43] A small shoulder peak located at 531.5 eV suggests that 5 wt% Nb_2O_5/Bi_2WO_6 is not the simple physical mixture of Nb_2O_5 and Bi_2WO_6, instead the chemical interaction exists between them. The characteristic peak of O 1s in 5 wt% Nb_2O_5/Bi_2WO_6 resulting from the overlapping contributions of Nb–O, Bi–O and W–O lattice oxygens. Combining with the results of XRD, SEM, FTIR, UV-vis and XPS, we are sure of the formation of heterojunction structure in Nb_2O_5/Bi_2WO_6.

3.2 Photocatalytic oxidative desulfurization performance

3.2.1 Selection of catalysts. Influences of the Nb_2O_5/Bi_2WO_6 compositions on the photocatalytic activities were investigated and the results were displayed in Fig. 6. The formation of heterojunction between two compounds suppressed the recombination of photogenerated electron–hole pairs and more photogenerated carriers would be generated for PODS due to the fast transport of the photoexcited electron–hole pairs at the interface of the heterojunction, which would greatly improve the activity.[44–46] Therefore, the heterojunction (1–10 wt%) Nb_2O_5/Bi_2WO_6 has much higher activities than the pure Bi_2WO_6 and Nb_2O_5. The activities of catalysts are associated with the amounts of deposited Nb_2O_5, the 5 wt% Nb_2O_5/Bi_2WO_6 has the highest photocatalytic activity and the desulfurization rate was approximately 99% after 120 min of visible light irradiation. Therefore, 5 wt% Nb_2O_5/Bi_2WO_6 was selected for further researches.

3.2.2 Kinetics of photocatalytic oxidative desulfurization. The photocatalytic oxidation of DBT was assumed to be the pseudo-first order reaction and the sulfur content of model fuel meets with eqn (3):

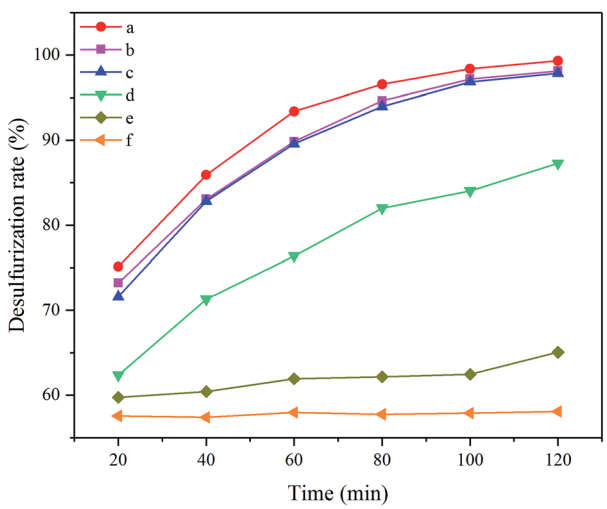

Fig. 6 Effect of different catalysts on desulfurization rate (a) 5 wt% Nb_2O_5/Bi_2WO_6; (b) 1 wt% Nb_2O_5/Bi_2WO_6; (c) 10 wt% Nb_2O_5/Bi_2WO_6; (d) Bi_2WO_6; (e) Nb_2O_5; (f) blank.

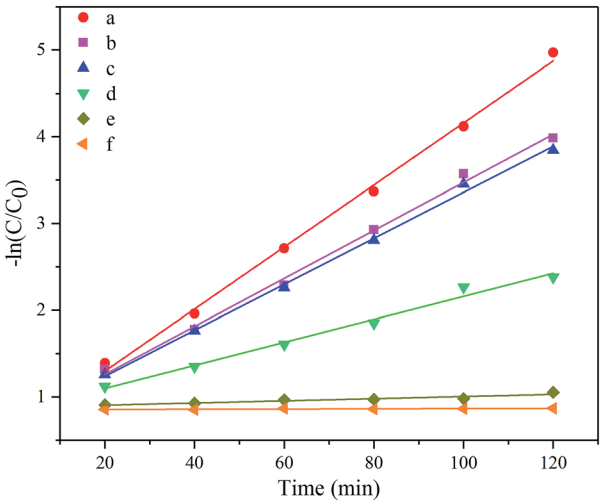

Fig. 7 Pseudo-first-order kinetic fitting curves for different catalysts (a) 5 wt% Nb_2O_5/Bi_2WO_6; (b) 1 wt% Nb_2O_5/Bi_2WO_6; (c) 10 wt% Nb_2O_5/Bi_2WO_6; (d) Bi_2WO_6; (e) Nb_2O_5; (f) blank.

$$-\ln C/C_0 = k \times t \quad (3)$$

C and C_0 have been explained in eqn (1), k is the pseudo-first-order reaction rate constant (min^{-1}).[47] The correlations of time-course variation of $-\ln C/C_0$ to the reaction time were represented in Fig. 7. Values of $-\ln C/C_0$ for all catalysts presented clear linear increases with the reaction time, suggesting the pseudo-first-order, which well proved the former assumption. Meanwhile, the reaction rate constants, the slopes of the straight lines, decrease in such order: 5 wt% Nb_2O_5/Bi_2WO_6 > 1 wt% Nb_2O_5/Bi_2WO_6 > 10 wt% Nb_2O_5/Bi_2WO_6 > Bi_2WO_6 > Nb_2O_5 > blank. Therefore, 5 wt% Nb_2O_5/Bi_2WO_6 was chosen as the efficient catalyst to make further researches.

3.3 Stability studies

Stability of 5 wt% Nb_2O_5/Bi_2WO_6 was studied in terms of its performance in every repeated run of PODS. As shown in Fig. 8A, the desulfurization rate still remains more than 90% after seven cycles of repeated PODS. The slight decrease in its activity can be attributed to the changes of catalysts in the recycle experiment. Furthermore, the XRD patterns of the 5 wt% Nb_2O_5/Bi_2WO_6 before and after PODS were displayed in Fig. 8B. It indicated that the used 5 wt% Nb_2O_5/Bi_2WO_6 had similar crystalline phase to that of the fresh one except the diffraction peak intensity decreased slightly. In brief, the catalyst does not exhibit significant loss of activity, indicating that the catalyst has good stability for photocatalysis.

3.4 Photocatalytic oxidative desulfurization mechanism

The radicals trapping experiment was conducted to well explain the photocatalytic mechanism. Active mediates including hydroxyl radicals ($^{\bullet}OH$), superoxide radicals ($^{\bullet}O_2^-$) and holes (h^+) were detected by adding isopropanol (IPA), *p*-benzoquinone (*p*-BQ) and disodium ethylenediaminetetraacetate (EDTA-2Na) to the reaction system, respectively. It can be observed in

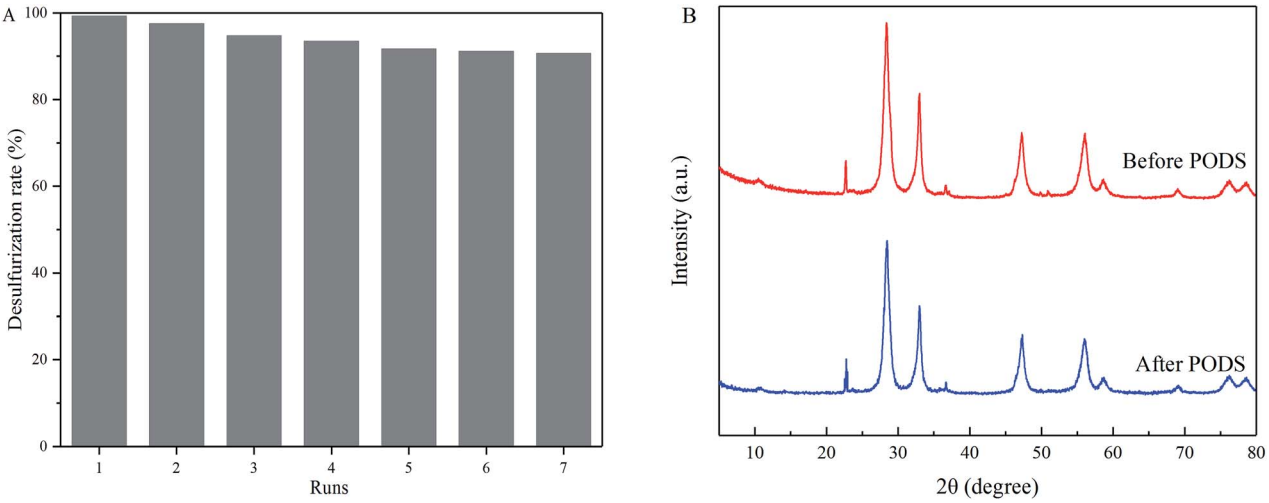

Fig. 8 (A) Desulfurization rates of 5 wt% Nb_2O_5/Bi_2WO_6 catalyst reused for different cycles; (B) XRD patterns of the fresh and used 5 wt% Nb_2O_5/Bi_2WO_6.

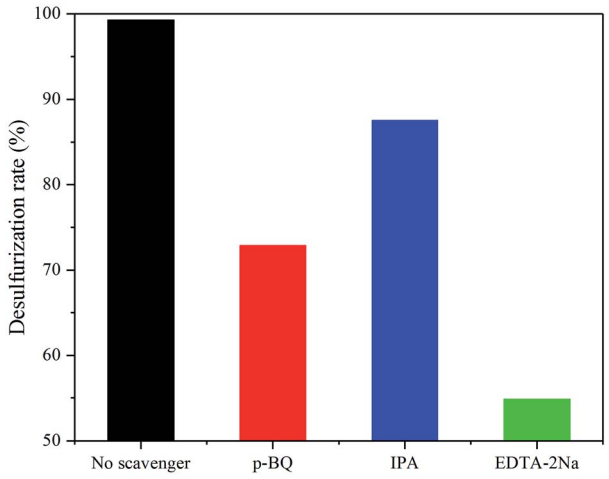

Fig. 9 Trapping experiments of active species under visible light irradiation in the presence of 5 wt% Nb_2O_5/Bi_2WO_6.

Fig. 9 that the desulfurization rates corresponding to four experiments, with no radicals trapping agent or with different radicals trapping agents, follow this order: no scavenger > IPA > *p*-BQ > EDTA-2Na. It was implied that the $^{\bullet}OH$ do not play a predominant role for the desulfurization. While $^{\bullet}O_2^-$ and h^+ are the main contributors to the sulfur removal in the catalytic system containing Nb_2O_5/Bi_2WO_6 heterojunction photocatalyst. Functions of the members in the PODS system were also investigated in Table 1, experiments were conducted with irradiation. Based on the desulfurization rates for systems with different combinations, the catalytic function of Nb_2O_5/Bi_2WO_6 is well proved. CH_3OH, acting as the solvent, plays an important role in the desulfurization after the efficient conversion of the DBT to polar sulfur compounds. In this one pot process, CH_3OH was added into the system simultaneously with all the other components, the formed polar sulfur compounds can be extracted in time, which is in favour of the proceeding of the reaction. In such PODS system Nb_2O_5/Bi_2WO_6, H_2O_2 and CH_3OH have a good synergistic effect and anyone of them is absolutely necessary.

An analysis of the oxidation product is of great importance in investigating the reaction mechanism. The model fuel before and after PODS and the used methanol were analysed with GC-

Table 1 Effect of different systems on the sulfur removal of DBT

Items	Conditions	Desulfurization rate (%)
1	H_2O_2 + DBT	12.24
2	CH_3OH + DBT	39.52
3	H_2O_2 + DBT + CH_3OH	41.14
4	H_2O_2 + DBT + Nb_2O_5/Bi_2WO_6	25.86
5	H_2O_2 + DBT + Nb_2O_5/Bi_2WO_6 + CH_3OH	99.31

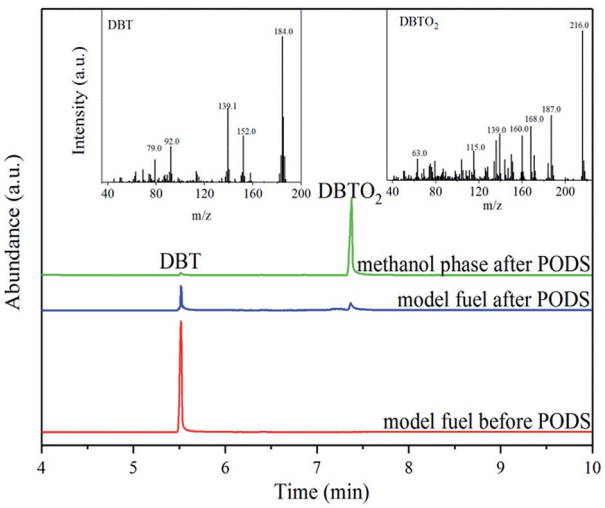

Fig. 10 GC-MS analysis of model fuel and the products for oil phase and methanol phase.

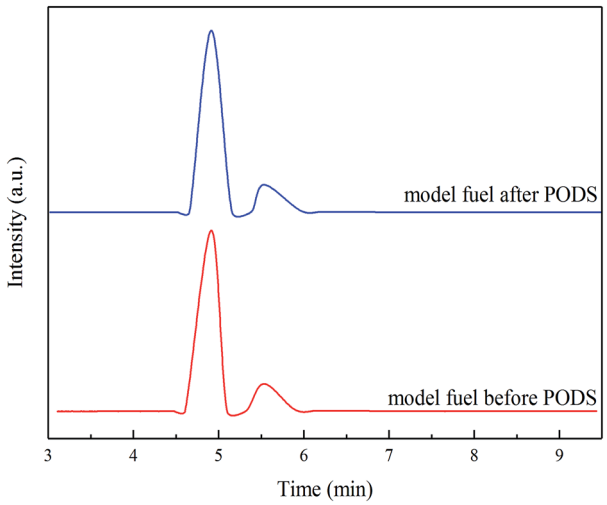

Fig. 11 GC patterns of model fuel before and after PODS.

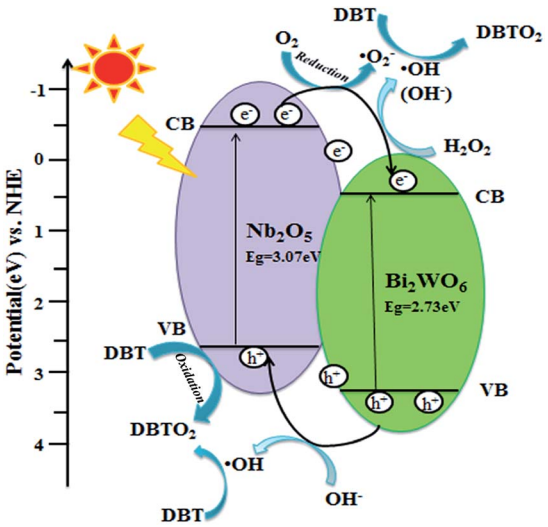

Fig. 12 The possible photocatalytic oxidation desulfurization mechanism on 5 wt% Nb_2O_5/Bi_2WO_6.

MS, and the results were shown in Fig. 10. Based on the MS results, dibenzothiophene sulfone ($DBTO_2$) is undoubtedly the only oxidation product of DBT. In PODS the extraction can effectively transfer $DBTO_2$ into the methanol phase, which is easily separated from the model fuel, thus the deep desulfurization was achieved.

In order to check whether the photocatalytic oxidation process damaged the hydrocarbons in the model fuel except the sulfur compound, the model fuel before and after PODS were detected by GC and the results were shown in the Fig. 11. The peaks were ascribed to the dodecane and its isomer in model fuel. Compared with the model fuel before PODS, the peaks of the model fuel after PODS almost have not changes, which illustrated PODS doesn't bring side effects on the composition of the hydrocarbon. Thus, PODS present a good selectivity for the removal of DBT in the dodecane.

Based on the above founding and the previous reports,[5,6,46,48] here we propose a possible mechanism for the PODS reaction on Nb_2O_5/Bi_2WO_6, as schematically shown in Fig. 12. For a semiconductor, the valence band (VB) and conduction band (CB) can be calculated according to the empirical equations:

$$E_{VB} = \chi - E^e + 0.5E_g \quad (4)$$

$$E_{CB} = E_g - E_{VB} \quad (5)$$

where E_{VB} is the valence band edge potential, E_{CB} is the conduction band edge potential, χ is the absolute electronegativity of the semiconductor, E^e is the energy of free electrons on the hydrogen scale (about 4.5 eV *vs.* NHE), and E_g is the band gap. The χ values for Nb_2O_5 and Bi_2WO_6 are 5.55 eV and 6.36 eV, respectively.[30,35] Thus, the E_{VB} of Nb_2O_5 and Bi_2WO_6 were calculated to be 2.59 eV and 3.22 eV *vs.* NHE, and the E_{CB} of them were determined to be −0.49 eV and 0.49 eV *vs.* NHE, respectively.

When the composite material is irradiated under visible light, the photogenerated electron injects to CB, while the hole is left on VB. It has been demonstrated that the CB and VB of Bi_2WO_6 and Nb_2O_5 are interlaced. Thus the hole and electron can transfer between the two phases. The photogenerated electrons on the CB of Nb_2O_5 efficiently transferred to CB of Bi_2WO_6, simultaneously the photogenerated holes effectively migrated from Bi_2WO_6 to Nb_2O_5, which suppresses the recombination process of photogenerated carries. In a reaction process, firstly, the reactant DBT adsorbed on the surface of Nb_2O_5/Bi_2WO_6 to form a surface charge transfer complex. Secondly, the photogenerated electron transferred to CB can quickly move and possess strong reducibility, such electron reacts with H_2O_2 and oxygen (O_2) dissolving in solution to form $^{\bullet}OH$ and $^{\bullet}O_2^-$ radicals.[48,49] DBT molecule was directly oxidized to the $DBTO_2$ by $^{\bullet}OH$ and $^{\bullet}O_2^-$ radicals. In addition, the photogenerated holes possess strong oxidizability, which can capture the lone pair electrons belonging to the sulfur atom of DBT molecule to forming $C_{12}H_8S^{\bullet+}$, and then further forming $DBTO_2$. Finally, the corresponding sulfones were extracted with methanol to achieve the purpose of deep desulfurization.

4. Conclusions

In summary, based on the interlaced CB and VB of Bi_2WO_6 and Nb_2O_5, novel Nb_2O_5/Bi_2WO_6 heterostructured composites materials were successfully synthesized *via* one-pot solvothermal route. It has the good stability, and it also exhibited better visible light photocatalytic activity than pure Bi_2WO_6 and Nb_2O_5 in PODS. Its synergistic effect with CH_3OH and H_2O_2 in the photocatalytic system accounts for the high desulfurization rates. In PODS, h^+ and $^{\bullet}O_2^-$ make more contribute than $^{\bullet}OH$ to the sulfur removal in the photocatalytic system containing Nb_2O_5/Bi_2WO_6 heterojunction photocatalyst, H_2O_2 and CH_3OH.

Conflicts of interest

There are no conflicts to declare.

Acknowledgements

This work was supported by Program for Liaoning Excellent Talents in University, abbreviated as 'LNET' (LJQ2015062), Program for Science and Technology Agency of Liaoning Province (20170540585), General Scientific Research Project of Liaoning Provincial Department of Education (L2015296, L2016018) and Science and Technology Planning project of Fushun (FSKJHT201376).

Notes and references

1 Y. Mathieu, L. Tzanis, M. Soulard, J. Patarin, M. Vierling and M. Molière, *Fuel Process. Technol.*, 2013, **114**, 81–100.
2 M. Masiol and R. M. Harrison, *Atmos. Environ.*, 2014, **95**, 409–455.
3 J. Han, X. Zheng, L. Zhang, H. Fu and J. Chen, *Environ. Sci.: Nano*, 2017, **4**, 834–842.
4 S. Li, S. Hu, K. Xu, W. Jiang, Y. Liu, Z. Leng and J. Liu, *J. Colloid Interface Sci.*, 2017, **504**, 561–569.
5 S. Li, S. Hu, J. Zhang, W. Jiang and J. Liu, *J. Colloid Interface Sci.*, 2017, **497**, 93–101.
6 X. Zheng and L. Zhang, *Energy Environ. Sci.*, 2016, **9**, 2511–2532.
7 L. Zhang, L. O. Herrmann and J. J. Baumberg, *Sci. Rep.*, 2015, **5**, 16660.
8 X. Zeng, X. Xiao, Y. Li, J. Chen and H. Wang, *Appl. Catal., B*, 2017, **209**, 98–109.
9 M. Zarrabi, M. H. Entezari and E. K. Goharshadi, *RSC Adv.*, 2015, **5**, 34652–34662.
10 L. Yun, Z. Yang, Z. B. Yu, T. Cai and Y. Li, *RSC Adv.*, 2017, **7**, 25455–25460.
11 X. Li, Z. Zhang, C. Yao, X. Lu, X. Zhao and C. Ni, *Appl. Surf. Sci.*, 2016, **364**, 589–596.
12 X. Lu, X. Li, J. Qian, N. Miao, C. Yao and Z. Chen, *J. Alloys Compd.*, 2016, **661**, 363–371.
13 W. Zhu, Y. Xu, H. Li, B. Dai, H. Xu, C. Wang, Y. Chao and H. Liu, *Korean J. Chem. Eng.*, 2014, **31**, 211–217.
14 C. Wang, W. Zhu, Y. Xu, H. Xu, M. Zhang, Y. Chao, S. Yin, H. Li and J. Wang, *Ceram. Int.*, 2014, **40**, 11627–11635.
15 S. Obregón and G. Colón, *Appl. Catal., B*, 2013, **140–141**, 299–305.
16 X. Li, F. Li, X. Lu, S. Zuo, C. Yao and C. Ni, *J. Alloys Compd.*, 2017, **709**, 285–292.
17 X. Chen, T. Yu, X. Fan, H. Zhang, Z. Li, J. Ye and Z. Zou, *Appl. Surf. Sci.*, 2007, **253**, 8500–8506.
18 R. Shao, Z. Cao, Y. Xiao, H. Dong and W. He, *RSC Adv.*, 2014, **4**, 26447–26451.
19 S. Qi, L. Fei, R. Zuo, Y. Wang and Y. Wu, *J. Mater. Chem. A*, 2014, **2**, 8190–8195.
20 S. Furukawa, A. Tamura, T. Shishido, K. Teramura and T. Tanaka, *Appl. Catal., B*, 2011, **110**, 216–220.
21 R. Shao, X. Zeng, Z. Cao, H. Dong, L. Wang, F. Wang, J. Liu, Z. Li and Q. Liang, *RSC Adv.*, 2015, **5**, 102101–102107.
22 J. Yan, G. Wu, N. Guan and L. Li, *Appl. Catal., B*, 2014, **152–153**, 280–288.
23 J. Xing, Z. Shan, K. Li, J. Bian, X. Lin, W. Wang and F. Huang, *J. Phys. Chem. Solids*, 2008, **69**, 23–28.
24 C. Mao, M. Li, Z. Fang, F. Meng, X. Qu, Y. Liu, M. Wang, J. Zhang, Z. Shi and X. Guo, *RSC Adv.*, 2013, **3**, 6631–6639.
25 X. Fan, X. Yue, J. Luo and C. Wang, *J. Nanopart. Res.*, 2016, **18**, 65–73.
26 X. Liu, Q. Lu and J. Liu, *J. Alloys Compd.*, 2016, **662**, 598–606.
27 J. Li, H. Hao, J. Zhou and Z. Zhu, *New J. Chem.*, 2016, **40**, 9638–9647.
28 Y. Zhang, L. Pei, Z. Zheng, Y. Yuan, T. Xie, J. Yang, S. Chen, J. Wang, E. R. Waclawik and H. Zhu, *J. Mater. Chem. A*, 2015, **3**, 18045–18052.
29 A. Xu, Y. Peng, Q. Chen, D. Wang and H. Zhou, *CrystEngComm*, 2015, **17**, 569–576.
30 F. Zhang, S. Zou, T. Wang, Y. Shi and P. Liu, *Photochem. Photobiol.*, 2017, 1–25.
31 Z. Liu, Q. Yu, J. Liu, T. Li and F. Huang, *Micro Nano Lett.*, 2017, **12**, 95–100.
32 Y. Xu, J. Song, F. Chen, X. Wang and H. Yu, *RSC Adv.*, 2016, **6**, 65902–65910.
33 J. Bao, S. Guo, J. Gao, T. Hu and L. Yang, *RSC Adv.*, 2015, **5**, 97195–97204.
34 H. Huang, K. Liu, K. Chen, Y. Zhang, Y. Zhang and S. Wang, *J. Phys. Chem. C*, 2014, **118**, 14379–14387.
35 Y. Hong, C. Li, G. Zhang, Y. Meng, B. Yin, Y. Zhao and W. Shi, *Chem. Eng. J.*, 2016, **299**, 74–84.
36 R. Shao, Z. Cao, Y. Xiao, H. Dong, W. He, Y. Gao and J. Liu, *RSC Adv.*, 2014, **4**, 26447–26451.
37 H. Lv, Y. Liu, J. Hu, Z. Li and Y. Lu, *RSC Adv.*, 2014, **4**, 63238–63245.
38 Z. Lin, J. Li, Z. Zheng, J. Yan, P. Liu, C. Wang and G. Yang, *ACS Nano*, 2015, **9**, 7256–7265.
39 J. Li, C. Yu, W. Fang, L. Zhu, W. Zhou and Q. Fan, *Chin. J. Catal.*, 2015, **36**, 987–993.
40 D. C. Castro, R. P. Cavalcante, J. Jorge, M. A. U. Martines, L. C. S. Oliveira, G. A. Casagrande and A. Machulek Jr, *J. Braz. Chem. Soc.*, 2015, **27**, 303–313.
41 W. Zhao, W. Zhao, G. Zhu, T. Lin and F. Xu, *Dalton Trans.*, 2016, **45**, 3888–3894.
42 Y. Pang, G. Xu, X. Zhang, J. Lv, K. Shi, P. Zhai, Q. Xue, X. Wang and Y. Wu, *Dalton Trans.*, 2015, **44**, 17784–17794.
43 W. Yang, B. Ma, W. Wang, Y. Wen and D. Zeng, *Phys. Chem. Chem. Phys.*, 2013, **15**, 19387–19394.
44 E. S. Aazam, *Ceram. Int.*, 2014, **40**, 6705–6711.
45 S. Li, X. Shen, J. Liu and L. Zhang, *Environ. Sci.: Nano*, 2017, **4**, 1155–1167.
46 S. Li, S. Hu, W. Jiang, Y. Liu and J. Liu, *J. Colloid Interface Sci.*, 2017, **501**, 156–163.
47 W. Zhu, G. Zhu, H. Li, Y. Chao and Y. Chang, *J. Mol. Catal. A: Chem.*, 2011, **347**, 8–14.
48 B. Sun, Y. Xue, L. Wang, L. Feng and C. Li, *J. Fuel Chem. Technol.*, 2016, **44**, 1074–1081.
49 W. Zhu, C. Wang, H. Li, P. Wu and S. Xun, *Green Chem.*, 2015, **17**, 2464–2472.

